Bachelor Thesis

Setup of a frequency-doubled high-power laser system in the blue for Rydberg atom spectroscopy

A cooperation between
5th Institute of Physics, University of Stuttgart
Institut für Halbleiteroptik und funktionelle Grenzflächen

University of Stuttgart
5th Institute of Physics

Marius Plach

06th March 2018

Revised version from May 2018

Examiner: Prof. Dr. Tilman Pfau

University of Stuttgart
5. Physikalisches Institut
Pfaffenwaldring 57, DE-70569 Stuttgart

Declaration

I hereby declare that this submission is my own work and that, to the best of my knowledge and belief, it contains no material previously published or written by another person, except where due acknowledgment has been made in the text.

Marius Plach
Stuttgart, 06th March 2018

Abstract

1. Deutsch

Im Rahmen dieser Arbeit wird der Aufbau eines optisch gepumpten Halbleiter-Scheibenlaser in Verbindung mit Frequenzverdopplung innerhalb des externen Resonators beschrieben. Der Laser soll für die Rydberg Spektroskopie im blauen Spektralbereich optimiert sein und eine hohe Ausgangsleistung von $P_{Out} \approx 5\,\mathrm{W}$ aufweisen. Hierfür wurde der Aufbau eines linearen Resonators realisiert. Durch optisches pumpen mit einem Diodenlaser konnte erfolgreich Laserlicht der fundamentalen Wellenlänge im nahen infrarot-Bereich erzeugt werden. Daraufhin wurden Messungen von Ausgangsleistung, Spektrum und Strahldurchmesser unter Variation der Parameter Chiptemperatur sowie Pumpleistung durchgeführt. Die Ergebnisse der Charakterisierung des Lasers wurden direkt in die Optimierung des Aufbaus umgesetzt und sind wegweisend für die weitere Anpassung der Chipstruktur. Als Projekt einer Kooperation zwischen dem 5. physikalischen Institut und dem IHFG profitieren beide Seiten gleichermaßen von den Erkenntnissen, die auf diesem Gebiet gemacht werden.

2. English

This thesis is about the setup of an optically pumped semiconductor disk laser in combination with intra-cavity frequency doubling. The laser is intended to emit light in the blue spectra with an output power of $P_{Out} \approx 5\,\mathrm{W}$ which can be used for Rydberg atom spectroscopy. In the design of a linear cavity we pumped a VECSEL with a $\lambda_{\mathrm{pump}} = 888\,\mathrm{nm}$ diode-Laser. We were able to receive stimulated emission of the fundamental laser wavelength in the near infra-red. This made it possible to conduct measurements of output power, spectra and beam diameter, dependent on the temperature of the chip or pump power. The results were directly implemented in an improvement of the existing setup. As a cooperation project between the 5th Institute of Physics and the IHFG both sides benefit from the know-how that is acquired.

Contents

List of abbreviations

AR Anti **r**eflective

AlAs Aluminium arsenide

AlGaAs Aluminium gallium arsenide ($Al_xGa_{1-x}As$)

BBO Beta barium borate $Ba(BO_2)_2$

CW **C**ontinous **W**ave

DBR **D**istributed **B**ragg **r**eflector

DFB **D**istributed **f**eed**b**ack (Laser)

DPSS **D**iode **p**umped **s**olid **s**tate

FPI **F**abry-**P**érot **i**nterferometer

FSR **F**ree-**s**pectral **r**ange

FWHM **F**ull **w**idth at **h**alf **m**aximum

GaAs Gallium arsenide

GaAsP Gallium arsenide phosphide ($GaAs_{1-x}P_x$)

HR **H**igh **r**eflective

IFSW **I**nstitut **f**ür **S**trahl**w**erkzeuge

IR **I**nfra-**r**ed

InGaAs Indium gallium arsenide ($In_xGa_{1-x}As$)

laser **L**ight **a**mplification by **s**timulated **e**mission of **r**adiation

LBO Lithium triborate LiB_3O_5

maser **M**icrowave **a**mplification by **s**timulated **e**mission of **r**adiation

PL **P**hoto**l**uminescence

QW **Q**uantum **w**ell

SiC Silicon carbide

SHG **S**econd **h**armonic **g**eneration

THG **T**hird **h**armonic **g**eneration

VCSEL **V**ertical-**c**avity **s**urface-**e**mitting **l**aser

VECSEL **V**ertical-**e**xternal-**c**avity **s**urface-**e**mitting **l**aser

Nd:YAG neodymium-doped yttrium aluminium garnet

1. Introduction

1.1. Motivation

Conventional laser[1] diodes operating at blue wavelengths are usually based on gallium nitride [1]. Such diode lasers do not offer the beam quality (profile) and divergence that is necessary for spectroscopy. Diode pumped solid state lasers with frequency doubled Nd:YAG[2]-emission or argon-ion lasers could be used in the blue as well [2] but they are expensive in acquisition as well as operating and difficult to be maintained. Additionally, they do not offer the possibility of fine tuning around the desired wavelength. Optically pumped semiconductor disk lasers with an intra-cavity frequency doubling promise benefits in those disciplines. Similar systems which work on this principle have already been investigated [3] but none of them achieved an output that meets the specifications our setup is intended for.

We pump optically using a high-power diode laser at a wavelength of $\lambda_{\text{pump}} = 888\,\text{nm}$ into a VECSEL[3] which is cooled by a Peltier element slightly below the room temperature. In the final shape of a Z-cavity, beam treatment parts such as birefringent filter and etalon are included. This makes possible to fine tune the fundamental wavelength in a defined range. A non-linear ß-BBO[4]-crystal is introduced for intra-cavity frequency doubling via critical phase matching. The achievement is to build a blue laser emitting with a tunable wavelength around $\lambda = 474\,\text{nm}$ and particularly high output power of $P_{\text{Out}} \approx 5\,\text{W}$ in a small overall size. Such a laser could be used for many purposes, especially in Rydberg atom spectroscopy.

A basis of the setup was laid by Richard Hermann during his bachelor thesis in 2017[4]. He managed to create a suitable VECSEL-chip as well as the parts of the setup itself.

[1] **L**ight **a**mplification by **s**timulated **e**mission of **r**adiation

[2] neodymium-doped yttrium aluminium garnet

[3] **V**ertical-**e**xternal-**c**avity **s**urface-**e**mitting **l**aser

[4] Beta barium borate $Ba(BO_2)_2$

2. Theory

2.1. Laser

The precise theoretical prediction of so called optical maser[1]s was published by A. Schawlow and C. Townes in 1958 [5] and the first laser was invented in 1960 as a solid-state ruby laser. The light of a laser has particular properties which makes it useful for scientific purposes, especially spectroscopy. To mention only the most important, it is monochromatic and available at countless different wavelengths, depending on the type of construction. It is comparatively intensive along a small diameter. The light has a large coherence length and is realizable as CW[2]-laser or pulsed.
A laser consists of three components: an active medium, a pump and the resonator.
The active medium can be a gas, liquid or a solid but has to offer the possibility to induce a population inversion. This is given when more electrons are in the excited state than in the ground state. Practically it requires at least three different energy levels since it is not possible to create a population inversion in a two-level-system. The pumping process would induce stimulated emission in the same quantity as it excites into the upper level which at most creates equilibrium. A third level from which the particles can relax continuously into the laser level makes a population inversion possible. The ideal system is a four-level system as it is shown in figure 2.1 The upper short-lived level is responsible for effective pumping and populating of the upper long-lived laser state. An inversion is created due to the rapid decay from level three to two. Between the long-lived state and the lower short-lived state the laser light emission is stimulated. In lower short-lived state the electrons drop down rapidly without radiation into the ground state. This makes this energy level depopulating fast and gains the inversion. The pump lifts the electrons into higher levels. Current injection as well as light of a gas discharge tube or diode are suitable power supplies for that purpose. From the long-lived level charge carriers can drop down into a lower state under emission of photons on two different ways. Spontaneous emission describes the transition

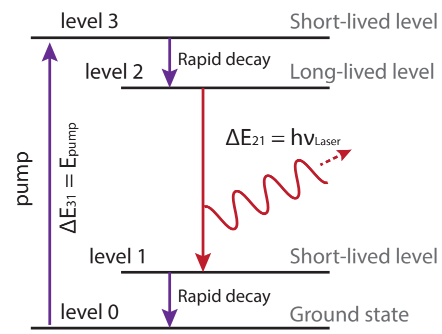

Figure 2.1.: Energy scheme of a four-level system. The wavelength of the emitted laser radiation depends on the energy difference between level two and one.

[1]**M**icrowave **a**mplification by **s**timulated **e**mission of **r**adiation
[2]**C**ontinous **W**ave

under emission of a photon which occurs at a random time. Stimulated emission is induced if an excited electron interacts with an incoming photon under emission of a photon with the same wavelength, polarization and orientation as the incoming. The resonator supplies a feedback of photons to generate stimulated emission and mode selection. Under given stimulated emission, the particles drop faster into lower levels than spontaneous emission can proceed. This is the reason why stimulated emission is predominating. Absorption and emission are mathematically described by the Einstein coefficients which were introduced by Albert Einstein in 1917 [6].

2.1.1. Diode laser

The diode laser consists of at least two layers of semiconducting material in which one is n-type doped while the other is p-type doped. If charge carriers are injected, they recombine with "holes" at the interface under emission of a photon of the wavelength that corresponds to the energy difference of the bandgaps. Figure 2.2 displays the basic three structures of laser diodes and the behavior of the charge carriers in conduction and valence band. To receive feedback, the sides of

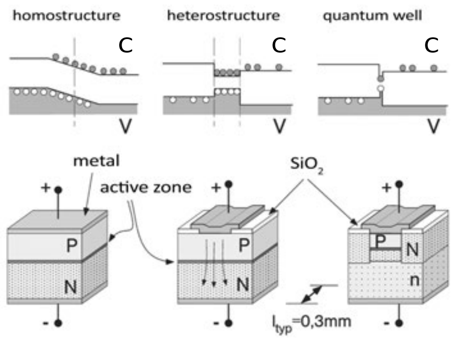

Figure 2.2.: Band structure and corresponding design of the diode. C stands for conduction band while V is the valence band. If charge carriers recombine at the barrier between the layers, photons are emitted. The heterostructure concentrates the inversion density on a certain point. The quantum well generates an active zone and an optical waveguide for the light. Slightly modified from [7].

the element are polished or coated in a way that photons get reflected and pass the active region several times before they leave. This gains the stimulated emission.

2.1.2. DPSS laser

The DPSS[4] laser is a solid-state laser, pumped with conventional laser diodes. Generally, solid state lasers can reach very high output powers due to the high energy density of population inversion that can be reached inside the solid. If higher power is necessary a pulsed output beam can be generated with mode-locking or a Q-switch. The latter increases temporarily the losses of the optical resonator to prevent feedback and stimulated emission. Due to the pumping, the population inversion goes on continuously and the amount of stored energy increases up to a maximum level that depends on the material. At this point the Q-switch immediately changes the resonator from low to high quality and stimulated emission is initiated. The stored energy discharges quickly in a short highly intensive beam pulse. DPSS laser are among to the strongest lasers that can be built and are used for material treatment or medical purpose. In our setup, a frequency doubled Nd:YAG laser is used to generate spontaneous emission [8].

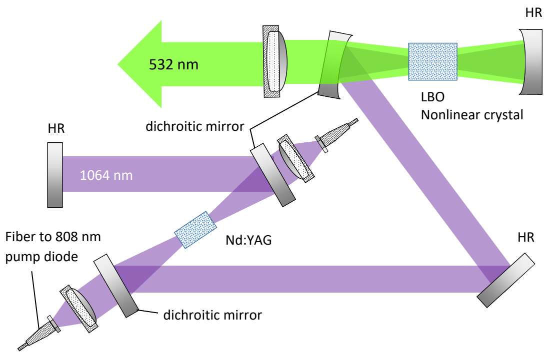

Figure 2.3.: Functional principle of a diode pumped solid state laser (DPSS). A LBO[3] crystal is used for frequency doubling.

2.1.3. VCSEL

VCSEL[5]s emit radiation from the surface. They are made of semiconducting materials with layer thicknesses in the range of nanometers and lateral extension in the size of a few microns. The cavity is embedded in layers with alternating indices of refraction forming Bragg mirrors (see DBR under 2.1.4). The advantage of

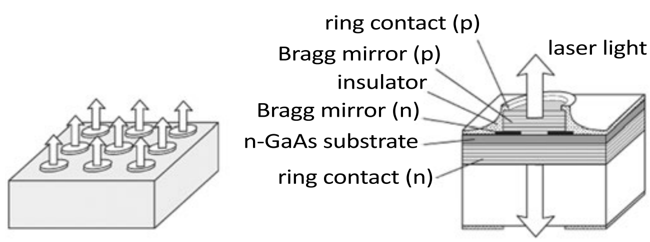

Figure 2.4.: Drawing of a VCSEL and electron microscope photograph of a real structure. Slightly modified from [7]

[4]**D**iode **p**umped **s**olid **s**tate
[5]**V**ertical-**c**avity **s**urface-**e**mitting **l**aser

this construction is a smaller beam divergence which causes a uniform light distribution and a higher efficiency when coupling into a fiber compared to edge-emitters.

2.1.4. Distributed Bragg reflector DBR

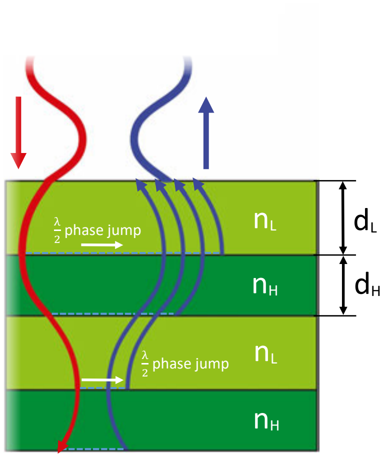

Figure 2.5.: Schematic drawing of the layer structure in a distributed Bragg reflector. Only one reflection and no back-reflections are considered to simplify the demonstration. The red wave is the incident beam while the blue represents the reflected ones.

A DBR[6] consists of layers with alternating high and low refractive indexes n_H/n_L. Each layer thickness is designed to have an optical path-length of one quarter of the refractive index dependent wavelength. At each transition the incident beam gets reflected. However, it receives a phase shift at the transition to the optically denser medium. This phase shift induces a superposition of reflected rays and altogether a reflection of the whole beam. Because of the wavelength-dependent design, a DBR is suitable for a certain range of wavelengths. Figure 2.5 is a schematic drawing of the functional principle of a DBR. In our chip design, AlAs[7] acts as a material with lower optical density while GaAs[8] has the higher refractive index. For reflection through constructive interference, the following equation must apply:

$$\frac{d_{\mathrm{L}} \cdot n_{\mathrm{L}}}{\lambda_0} = 1/4 = \frac{d_{\mathrm{H}} \cdot n_{\mathrm{H}}}{\lambda_0} \tag{2.1}$$

Thickness of a layer	$d_{\mathrm{L/H}}$	**Wavelength**	λ_0
Refractive index low/high	$n_{\mathrm{L/H}}$		

The DFB[9] laser is similar to a laser with DBRs. Here, the active zone itself acts like a reflector while the DBR is located outside the active zone.

[6]**D**istributed **B**ragg **r**eflector
[7]Aluminium arsenide
[8]Gallium arsenide
[9]**D**istributed **f**eed**b**ack (Laser)

2.1.5. VECSEL

The difference between a VCSEL and VECSEL is that the latter has the second cavity mirror outside of the semiconductor material, far away from the active region. The first reflector is given by a DBR (see 2.1.4). Due to the fact that the second mirror can be located far away from the active medium, there are different ways to arrange a cavity (see 3.1). Additionally, beam-changing components can be placed inside the optical path. An optical pump illuminates wide areas of the chip surface. This increases the maximum pump power and leads to a better beam quality. The active region consists of alternating doped layers with high and low band gaps. The former is called *barrier* while the latter are named *quantum wells*. QW[10]'s can be mathematically described as a one-dimensional quantum pot. Changing The thickness of the layer affects the width of the quantum pot while the ratio of doping atoms changes its height. In this way, the propagating wavelength of a VECSEL can be adjusted in a wide range, limited by the stability of the structure which strongly depends on the doping. Using the corresponding wavelength, it is possible to pump both, quantum wells and barriers but directly pumping into quantum wells induce less heat. This is caused by the lower quantum defect, dependent on the energy difference between pump- and emitted wavelength. The layers are epitaxially grown, a procedure in which a molecular beam is used to place thin layers in the size of nanometers. The elaboration of a structure for the epitaxy procedure is part of Richard Hermann's Bachelor thesis [4]. The layer sequence can be found in the appendix A.

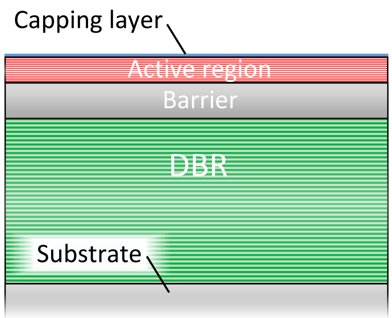

Figure 2.6.: Schematic structure drawing of the VECSEL chip in the proportion of our sample structure W00735. The substrate is the largest part of the chip and approximately 10 times thicker than the DBR.

2.2. Frequency doubling - SHG

Frequency doubling, also termed SHG[11] is the act of generating light of the doubled wavelength of a high intensive fundamental mode. SHG makes it possible to use existing laser systems to generate radiation in a completely different wavelength area. This opens innumerable possibilities

[10]**Q**uantum **w**ell
[11]**S**econd **h**armonic **g**eneration

since other types of lasers, such as diode lasers, are not available in corresponding frequency ranges or have a comparatively poor beam quality. The process can be described by two photons of the fundamental wavelengths, which combine to a photon of doubled energy that is equal to half of the wavelength (Figure 2.7).

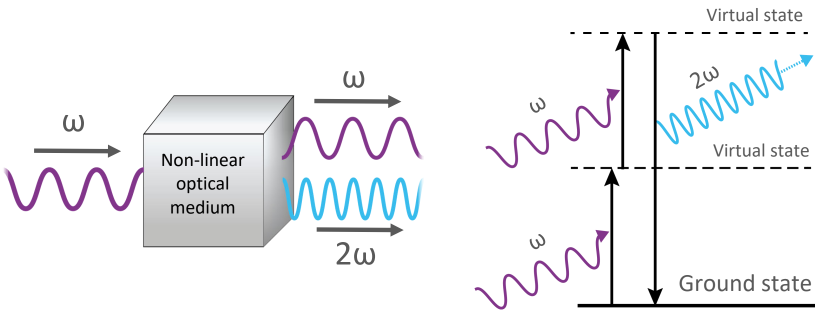

Figure 2.7.: Left: Frequency doubling with a non-linear optical medium. Right: Energy scheme of SHG. Two photons are excited into virtual states and a wave with the doubled frequency is generated during the drop down. The purple wave represents the fundamental mode while the blue is the second harmonic.

Successful SHG requires that the refractive index of the fundamental and the second harmonic is the same:

$$n_\omega = n_{2\omega} \tag{2.2}$$

This is called phase matching. An incorrect phase matching causes a destructive interference which reduces the intensity of the second harmonic. Using the Sellmeier equations [7] and the ß-BBO specific Sellmeier parameters [9] one can calculate the refractive index depending on the wavelength for the extraordinary and the ordinary beam. The difference between the refractive indexes of ordinary and extraordinary beam is reasoned in the unavoidable dispersion of any material. Phase matching is achieved by aligning the BBO-crystal in a certain angle to the incident beam. This changes the refractive index of the extraordinary beam to the value of the ordinary beam which stays the same. The phase matching angle can be calculated with [7]:

$$\sin^2\theta_{\mathrm{PM}} = \frac{n_{\mathrm{o}}^{-2}(\omega) - n_{\mathrm{o}}^{-2}(2\omega)}{n_{\mathrm{e}}^{-2}(2\omega) - n_{\mathrm{o}}^{-2}(2\omega)} \tag{2.3}$$

Phase matching angle	θ_{PM}	**Refractive index ordinary/extraordinary**	$n_{\mathrm{e/o}}$

For an achieved SHG of $\lambda_{\mathrm{SHG}} = 474\,\mathrm{nm}$ the phase matching angle is calculated to [7]:

$$\theta_{\mathrm{PM}} = \arcsin\sqrt{\frac{n_o^{-2}(948\,\mathrm{nm}) - n_o^{-2}(474\,\mathrm{nm})}{n_e^{-2}(474\,\mathrm{nm}) - n_o^{-2}(474\,\mathrm{nm})}} \tag{2.4}$$

$$\theta_{\mathrm{PM}} = \arcsin\sqrt{\frac{1.6576^{-2} - 1.6811^{-2}}{1.5600^{-2} - 1.6811^{-2}}} = 24.9^{\circ} \tag{2.5}$$

This is the angle in which the fundamental beam of $\lambda_{\mathrm{Fun}} = 948\,\mathrm{nm}$ incidents for phase matching and successful SHG in a procedure called critical phase matching. An AR[12]-coating avoids too high losses due to reflections by the incident beam. To calculate the refractive index of the extraordinary ray at a certain angle, the following equation is used [7]:

$$\frac{1}{n^2(\theta)} = \frac{\cos^2\theta}{n_o^2} + \frac{\sin^2\theta}{n_e^2} \tag{2.6}$$

The refractive index plotted over wavelength at phase matching angle is plotted in figure 2.8.

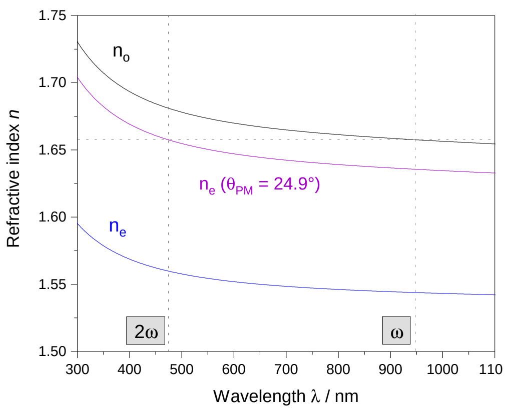

Figure 2.8.: Refractive index of ordinary (n_o) and extraordinary (n_e) beam in ß-BBO for vertical incident. Additionally, the extraordinary beam incident in the phase matching angle θ_{PM} is plotted. Under this angle the refractive index of the fundamental mode at $\lambda_{\mathrm{Fun}} = 948\,\mathrm{nm}$ is the same as the second harmonic at $\lambda_{\mathrm{SHG}} = 474\,\mathrm{nm}$.

A material with refractive indexes which are temperature-dependent (for example $NKbO_3$) can be used for phase matching via temperature tuning, termed non-critical phase matching. For our setup a thermal stability of the nonlinear medium is important for steady operating. Additionally, a high transmission at the corresponding wavelengths ensure that the radiation is not absorbed. Both is given with ß-BBO.

We consider the case of weak conversion when the fundamental mode is only slightly weakened which is the case passing BBO. Furthermore, we suppose perfect phase matching. The Intensity of the SHG increases continuously with the length of the crystal [7]:

[12] **A**nti **r**eflective

$$I_{\mathrm{SHG}} = \Gamma^2 I_{\mathrm{Fun}}^2 l^2 \tag{2.7}$$

Intensity of the SH	I_{SHG}	**Intensity of the fundamental**	I_{Fun}
Conversion coefficient	Γ	**Crystal length**	l

The conversion coefficient is a wavelength-specific material-dependent value. In practice, the crystal length l is limited by the focus of a Gaussian laser beam and a compromise between strong, constant intensity and the length of the medium. Since the BBO is placed intracavity in our setup, multiple pass increases the intensity and the effective length.

2.3. Birefringent filter

A birefringent filter consists of one or more plates of a birefringent material such as crystalline quartz. The axis-dependent refractive index of these materials split the incident beam into ordinary and extraordinary rays. The two rays pass with different velocity and interfere at the output. By rotating the plate, the refractive index of the extraordinary ray changes and thereby its velocity while the ordinary ray stays the same. The transmission peak is at the maximum when constructive interference between the rays occurs. This is given under the condition [7]:

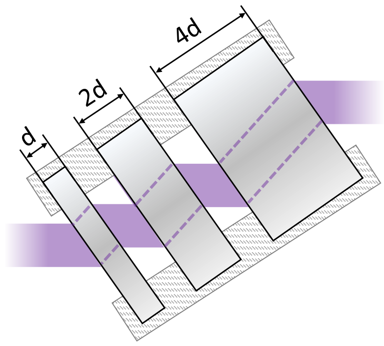

Figure 2.9.: Birefringent filter cascade of three plates, also termed Lyot filter arranged in the Brewster angle. The thickness of each plate is doubled.

$$2\pi(n_{\mathrm{o}} - n_{\mathrm{e}})d\big/\lambda = \Delta\varphi = 2\pi m \quad ; m \in \mathbb{Z} \tag{2.8}$$

Refractive index	$n_{\mathrm{o/e}}$	**Plate thickness**	d
Wavelength	λ	**Phase change**	$\Delta\varphi$

To supress any other wavelengths except for the main mode of the laser, the light which can pass the plates has to be linear polarized. Therefore, the birefringent material is embedded between two polarization filters or, to avoid losses by polarizers, arranged at the Brewster angle to the incident beam. On this way, the s-polarized light gets reflected while the p-polarized passes. For the intensity of a linear one-axial polarized beam the transmitted intensity is (according to [7]):

$$I_T = I_0 \left(\cos^2\left(\frac{(n_o - n_e)\pi d \nu}{c}\right) + \sin^2\left(\frac{(n_o - n_e)\pi d \nu}{c}\right) \cos^2(2\Phi) \right) \tag{2.9}$$

Transmitted/initial intensity	$I_{T/0}$	**Light velocity**	c
Azimuthal angle about the filter plate axis	Φ	**Frequency**	ν

The maximum intensity is achieved for $\Phi = 45^\circ$ with a FSR[13] of $\Delta\nu = c/d(n_0 - n_e)$. The thinner the birefringent plate is, the longer is the FSR and the broader FWHM[14]. To realize a large FSR with a narrow FWHM multiple birefringent plates are arranged in series (see figure 2.9).

Additionally, an etalon can be placed inside the optical path of the cavity. It consists of a quartz crystal with two reflecting surfaces. The transmitted wavelength strongly depends on the optical path which is changed by the angle of the incident beam. If the optical path is an integer multiple of the wavelength, transmission is given. Thus, the wavelength can be selected by rotating the etalon. The functional principle is the same as a FPI[15] where two parallel high reflecting mirrors are used with a gap between.

[13]**F**ree-**s**pectral **r**ange
[14]**F**ull **w**idth at **h**alf **m**aximum
[15]**F**abry-**P**érot **i**nterferometer

2.4. Fresnel equations

The Fresnel equations describe reflection and transmission of electromagnetic waves at the transition between two media. Presuming Snell's law and a complex refractive index, they can be formulated as follows [11]:

$$r_s = \frac{\frac{Ni}{\mu_i}\cos\theta_i - \frac{N_t}{\mu_{rt}}\cos\theta_t}{\frac{Ni}{\mu_i}\cos\theta_i + \frac{N_t}{\mu_{rt}}\cos\theta_t} \qquad r_p = \frac{\frac{Nt}{\mu_t}\cos\theta_i - \frac{N_i}{\mu_{ri}}\cos\theta_t}{\frac{Ni}{\mu_i}\cos\theta_i + \frac{N_t}{\mu_{rt}}\cos\theta_t} \tag{2.10}$$

Reflectivity index	$r_{s/p}$	**Complex refractive index**	N_i
Incident/emergent angle	θ_i/θ_t	**Permeability**	$\mu_{ri/rt}$

Only the formulae for the reflection are mentioned. r_s stands for the vertical polarized reflective index of the beam and r_p is the index of parallel polarized radiation. A frequently upcoming case is given if the media are dielectric $N_i = n + i\kappa_i \longrightarrow N_i = n_i$:

$$r_s = -\frac{\sin(\theta_i - \theta_t)}{\sin(\theta_i + \theta_i)} \qquad r_p = \frac{\tan(\theta_i - \theta_t)}{\tan(\theta_i + \theta_i)} \tag{2.11}$$

In order to receive the reflectivity, the reflectivity index has to be squared:

$$R_{p/s} = r_{p/s}^2 \tag{2.12}$$

Using this formula, we can make predictions about the reflection of the present setup. As we want to have a high energy density in the active zone, a low reflection of the chip/heatspreader needs to be achieved.

3. Experimental setup

The following chapter consists of an explanation of the setup used during this thesis. It begins with a description of different cavity shapes and is followed by a detailed description of the applied parts. Under 3.2.1 it is explained how to investigate the beam diameter of the pump laser which is an important parameter for the energy density in the active region of a VECSEL. The last part is about the bonding of VECSEL chips, which plays a major role for the heat dissipation that is always a critical issue in high-power systems.

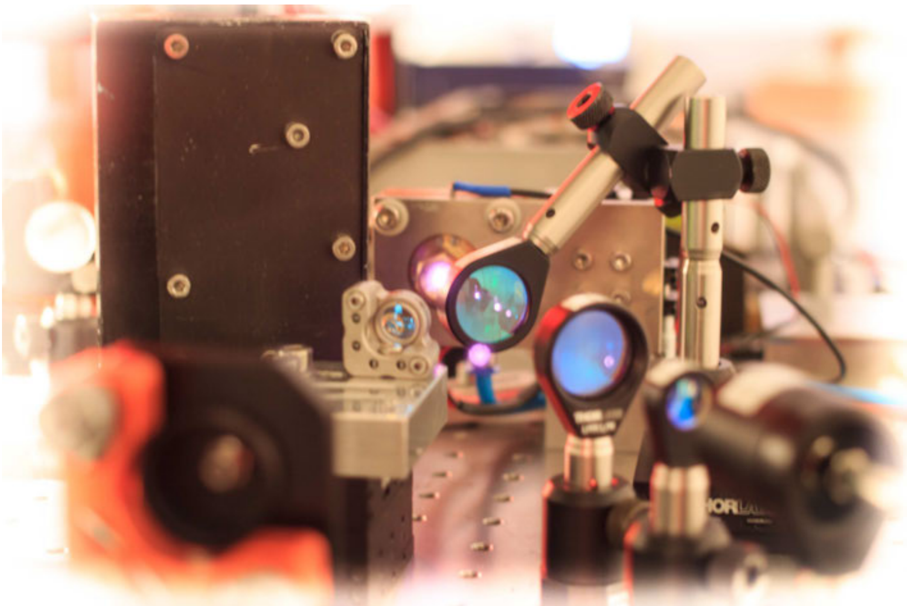

Figure 3.1.: Picture of our setup, taken with a DSLR camera with weak IR[1]-Filter. The pump beam is slightly visible as purple radiation. On the right hand one can see the pump optics. The bright dot in the middle is the chip holder with the external cavity mirror on the opposite. One can see the beam blocker in the back of the picture on the left-hand side and the fiber coupler for the spectrometer in the front.

3.1. Cavity shapes

Working with a VECSEL allows different arrangements of the cavity which must consist of at least one external resonator mirror. The simplest structure is a **linear cavity** (see figure 3.2). In this case, all elements of the setup are fixed along one axis. The single resonator mirror is parallel to the DBR and can be aligned easily. This setup is sufficient for the first checks of the parts and VECSEL structure. Because the light of the SHG is absorbed by the chip, an intra-cavity frequency doubling is not possible.

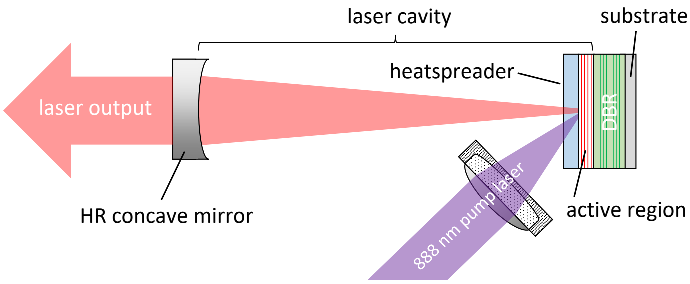

Figure 3.2.: Schematic drawing of the setup for a linear cavity. The concave mirror is highly reflective for the fundamental laser wavelength to provide stimulated emission.

The **V-Cavity** (figure 3.3) has the shape of a V which means that a concave fold mirror is used to construct an arm in which the BBO can take place. It is that the mirrors are dichroitic

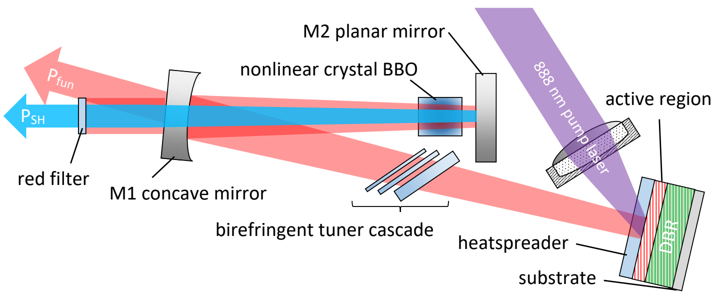

Figure 3.3.: Setup of a V-cavity for second harmonic generation. The concave mirror M1 is highly reflective for the fundamental mode. The second harmonic which is created in the BBO-crystal can pass the Mirror M1. The planar Mirror M2 is highly reflective coated for both wavelengths.

and transmit the light generated by the non-linear crystal. Otherwise, the radiation would be reflected into the VECSEL and absorbed. The V-cavity already offers place for some further parts for beam treatment like a birefringent filter. This is essential to force the laser into single-mode

regime and tune the wavelength in a certain range.
The most complex shape compared to the former ones is the **Z-cavity** (figure 3.4). Two fold and one planar mirror form the external cavity. This structure is difficult to align due to the certain angles and distances that have to be adjus t offers huge space to place various beam treatment elements in the optical path su lter and BBO crystal. The plan is to

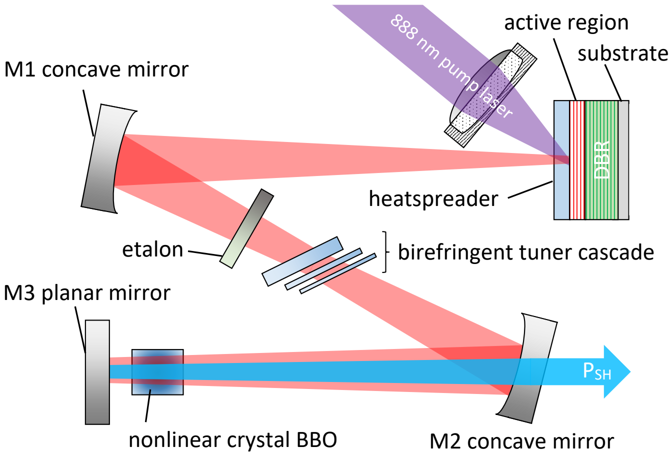

Figure 3.4.: Schematic setup of a Z-cavity with a birefringent tuner cascade and an etalon in the optical path. All mirrors M1 to M3 are high reflective coated except for the concave mirror M2 which transmits the second harmonic (SH).

first implement the construction of a linear cavity and then convert into a V-Cavity. Finally, the setup should be in the form of a Z-cavity. The whole setup in this shape will have the size of a shoebox which is, compared to existing systems, quite small.

3.2. Setup

Our setup consists of a fiber-coupled diode laser *"BrightLase Ultra-50"* by *QPC Lasers* with a wavelength $\lambda_{\text{pump}} = 888\,\text{nm}$. It can reliably deliver pumping powers up to $P_{\text{Pump}} = 35\,\text{W}$. The high-power fiber has a core diameter of $d_{\text{Core}} = 200\,\mu\text{m}$ which means that it is a MM-fiber that is generally not polarization-preserving. In a linear cavity there is only one mirror and one axis in which the cavity length can be varied. This makes the system easy to align. Figure 3.5 shows the schematic setup as it was used for the PL[2] measurements. The beam blocker is an important

[2] **P**hoto**l**uminescence

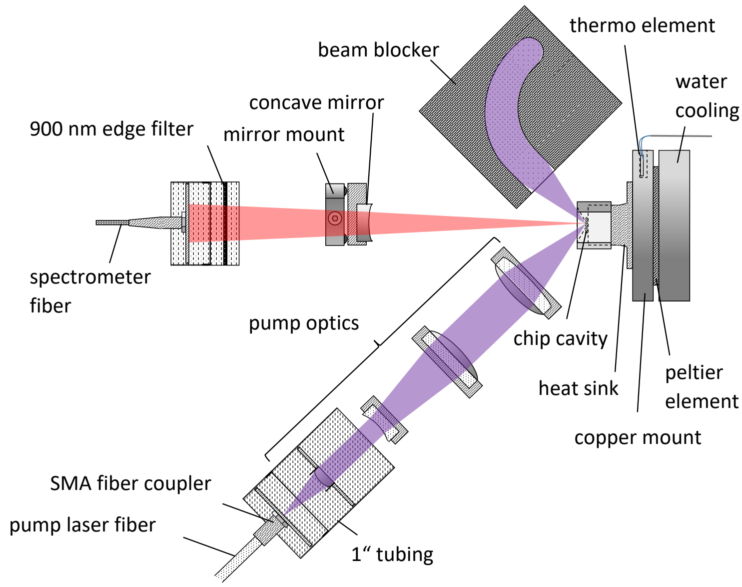

Figure 3.5.: Setup for PL measurements of the VECSELchip. Either the path of the pump beam (purple) and the light gained through stimulated emission from the chip (red) are visualized.

protection since the system is pumped with high power and the sample reflects a significant ratio of the incident radiation. A concave mirror which reflects the pump beam back to pass the chip a second time has been considered.

3.2.1. Determination of the beam diameter

The beam diameter and the power are two factors which determine the energy density inside the active region of the VECSEL chip. The smaller the diameter is, the more stimulated emission can be obtained. Therefore, the diameter of the incident pump beam must be scaled down.
For determination of the beam diameter a CCD camera is used. We took a *Thorlabs DCC1545M* which, by using the delivered software, displays the picture directly on the computer screen with an intensity profile along a self-set line. The focus point is investigated by moving the camera to the position where the diameter becomes larger shifting in both directions. Furthermore, the power of the pump laser was decreased until the intensity at the camera did not saturates anymore. Then a picture was taken. To calculate the beam diameter, we determine the background noise

and maximum of the peak to calculate the difference and get the real maximum.

$$I_{\text{Max}} = \text{Max}(I_{(x)}) - I_{\text{Background}} \tag{3.1}$$

Afterwards we divide this value by e^2 and add the background noise.

$$I_{\text{Width}} = \frac{I_{\text{Max}}}{e^2} + I_{\text{Background}} \tag{3.2}$$

Now we locate the two-pixel positions right and left to the center and multiply the difference of them with the pixel size as mentioned in the manual. For the Thorlabs DC1545M one pixel is equal to 5.2 μm [12].

$$D_{\text{Beam}} = (x_{\text{Width right}} - x_{\text{Width left}}) \cdot d_{\text{Pixel}} \tag{3.3}$$

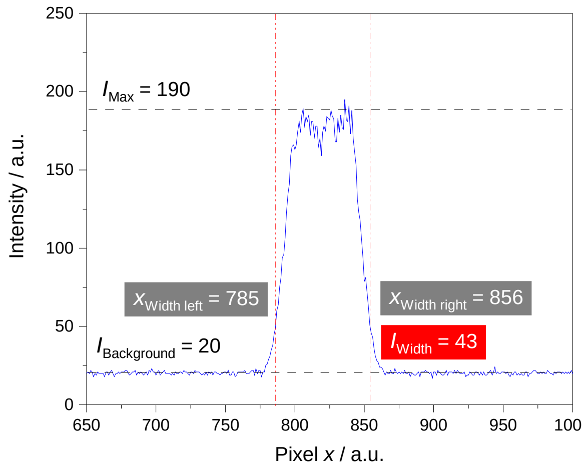

Figure 3.6.: Pump laser beam profile along the set line through the picture of the beam. With the background intensity and the maximum beam intensity the beam diameter is calculated.

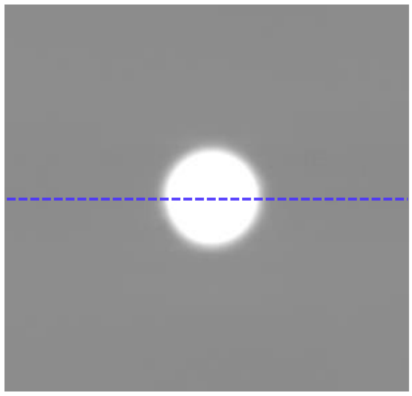

Figure 3.7.: Raw picture of the beam, taken with a Thorlabs DCC1545. The blue line is positioned in the middle of the beam. The intensity along this line gets analyzed.

Because the light passed through a multimode fiber, it is no longer Gaussian. In the example which is plotted in figure 3.6 the beam width is calculated with equations (3.2) to (3.6) to

$$D_{\text{Beam}} = (x_{\text{Width right}} - x_{\text{Width left}}) \cdot d_{\text{Pixel}}$$
$$D_{\text{Beam}} = (856\,\text{px} - 785\,\text{px}) \cdot 5.2\,\mu\text{m}/\text{px} = 369\,\mu\text{m}$$

To reach sufficient energy densitys inside the active region and a low VECSEL threshold, a diameter of $D_{\mathrm{Beam}} \approx 150\,\mu\mathrm{m}$ is desired.
The first lense package of the system consisted of two simple plano-concave lenses. One for collimation after outcoupling of the fiber and the second to focus the beam on the VECSEL. The shorter the focal length of the focus lense is, the sharper becomes the focus point. Therefore, we took a plano-concave lense with $f = 18.40\,\mathrm{mm}$ for focusing. By varying the distances of the lens system we were able to scale down the beam diameter to a value of $D_{\mathrm{Beam}} = 244\,\mu\mathrm{m}$. The insuperable problem at this configuration was a too small distance between lens and VECSEL chip. The lens blocked the optical path of the external cavity. Furthermore, with a simple plano-concave lens it is in theory not possible to lower less than the diameter of the multimode fiber $D_{\mathrm{Fiber}} = 200\,\mu\mathrm{m}$ due to linear ray optic laws.
By constructing a Galilean telescope, the minimum diameter can be reduced. A Galilean telescope consists of a plano-concave divergent lens that spreads the beam and a convergent plano-convex lense for focusing. The arrangement of the lenses leads to a magnification which makes it possible to scale down smaller than the fiber diameter. The software " *Zeemax OpticStudio 17*" offers the possibility to calculate the estimated beam behavior by using the laws of linear optics and specific data of the most conventional lenses on the market. This made it possible to simulate and optimize the distances and provide a setup for the desired diameter. With the simulated Galilean telescope for pump beam optics, we were able to receive a value of $D_{\mathrm{Beam}} = 322\,\mu\mathrm{m}$. This is larger than before but offers enough distance to the VECSEL chip. Furthermore, this value does not accord with the theoretical predictions. This could be caused by an inaccurate adjustment or aberrations of the lenses. However, the value was sufficient for the first laser activities but a further improvement should be kept in mind.

3.2.2. VECSEL chip bonding

The heatsink is the part of the construction on which the chip is mounted. It conducts the heat from the chip surface to a Peltier element which is coupled to water cooling. As it is calculated in section 4.4.5, a minimum heat output of $P_{\mathrm{heat}} = 1.25\,\mathrm{W}$ is induced in the tiny area of the beam diameter at full pump power. The Peltier element manages the temperature of the chip holder and is controlled by a microcontroller. It is necessary that the heatsink is made of a material with a high thermal conductivity. In our case the heatsink is made of brass, an alloy of copper and zinc with good properties in stability and thermal behavior. Nevertheless, copper has an even higher thermal conductivity but cannot be used because of its softness. Fine threads could be easily turned over and parts of the construction could get bend under pressure. The backside of the chip is bonded to the heatsink with one layer of indium, a soft material with relative high

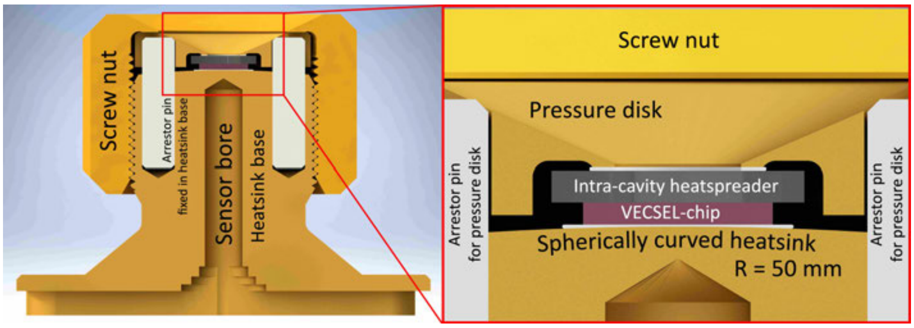

Figure 3.8.: Design of the chip holder used in our setup taken from [13] with a detailed cutout around the VECSEL chip. The pump laser beam incidents from the top through a cylindrical opening in the pressure disk. The shape of the pressure disk as well as the two arrestor pins limit the size of the intra-cavity heat spreader. The white layer between heat spreader and pressure disk as well as underneath the chip is indium.

thermal conductivity. It easily fills the small gaps on the surface of chip and heatsink and acts as a thermal connection. For the same reason there is another layer of indium between the heat spreader and the pressure disk. By turning the screw-nut of the chip holder, the force between heat spreader and chip is increased up to the level where indium gets molded. It takes almost 24 hours after a pressure quench until the indium is no longer mobile. During this time the screw must be turned again to gradually ensure a firm contact between chip and heat spreader. The radius of the heatsink, in our case $r_{\text{Heatsink}} = 100\,\text{mm}$, puts pressure in the middle of the chip. Previous attempts with a curvature of $r_{\text{Heatsink}} = 50\,\text{mm}$ lead to chip cracks during the bonding process (figure 3.10). In the case of cracking, there is insufficient contact between the chip and the SiC[3] heat spreader (see figure 3.9) resulting in a loss of thermal conduction and opacity. The well-focused high-power pump beam spot can result in a local thermal destruction of the chip. In addition, the combustion gas induces unwanted transparency reducing coatings on chip and heat spreader.

Table 3.1.: Thermal conductivity of the most common chip holder materials.

Heatsink materials		Bonding materials		Heatspreader materials	
Material	Conductivity W/m k	Material	Conductivity W/m k	Material	Conductivity W/m k
Brass [14]	120 - 250	Indium [15]	81.6	4H-SiC [16]	490
Copper [15]	401	Silver [15]	429	Diamond [15]	$0.99 \ldots 2.32 \cdot 10^3$

[3] Silicon carbide

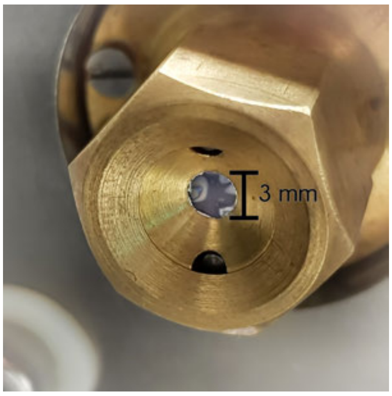

Figure 3.9.: Chip holder with a cracked chip inside the chip cavity. In the bright areas there is no sufficient contact between heat spreader and VECSEL. No emission can be expected and the chip will be destroyed by focusing the pump beam on those spots.

Figure 3.10.: Heatsink with removed screw-nut and heat spreader. Cracks in the VECSEL-chip occurred during the bonding process are clearly visible. Underneath the chip one can see the indium for the bonding.

The thermal conductivity of indium as a bonding material is lower than that one of heatsink materials like copper or brass (dependent on the copper/zinc ratio of the alloy). Heatspreader materials such as 4H-SiC and diamond have a conductivity in the same order of magnitude. Although the indium layer is thin, a better thermal conductivity could probably delay the point of thermal rollover. Alternatively, thin layers of pure silver or alloys, which are usually softer could be used in future. Further experiments are still pending. Table 3.1 gives an overview about the most common materials which are used for the chip holder construction.
Another bonding method is the so-called liquid capillarity bonding. A thin film of a liquid (e.g. water, isopropanol) is added to the VECSEL chip. Heatspreader and chip are carefully placed on each other while the surface is wet. After the liquid is evaporated, only Van-der-Waals-forces make chip and heat spreader stick together, without any external pressure that could harm the chip [17].

4. Results

4.1. Pump laser, fiber and characterization

The fiber we use in this setup is a multimode fiber with a core diameter of $d = 200\,\mu m$. A MM[1]-fiber is not preserving the polarization of a beam. By comparing the data of the diode pump laser given in the datasheet with the power that we could measure with a powermeter (see fig. 4.1), a discrepancy was detected. After some trials it turned out that the fiber end on the side of the diode laser was molten (see figure 4.2). This occurs when scratches or dust covers the input and a high power laser beam couples in. The broken fiber was replaced by a new one with the same specifications. Another power measurement of the pump-laser was made. Using the new fiber, the measurements matched the expected value from the datasheet up to the limit of the power supply.

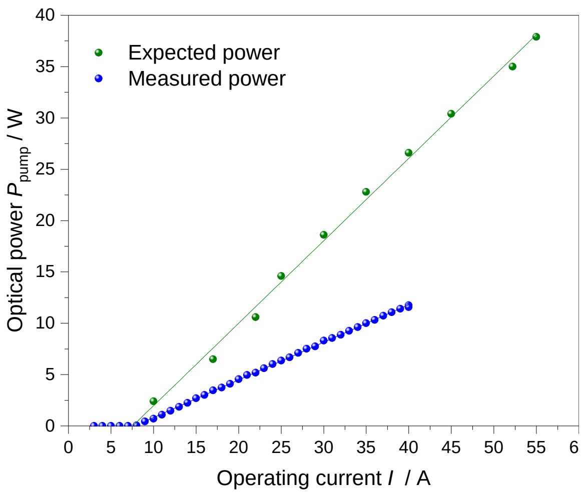

Figure 4.1.: Optical output power of the fiber (blue) depending on the operating current. The green line represents the values from the laser datasheet.

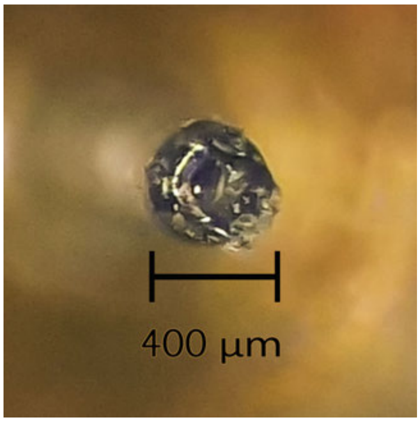

Figure 4.2.: A molten fiber input with droplets on the surface. The beam cannot be coupled into the fiber.

A linear fit was made by the measurements of the optical power plotted over the operating current (figure 4.3). This fit offers the possibility to calculate the optical power depending on the current, adjustable at the power supply.

[1]Multimode

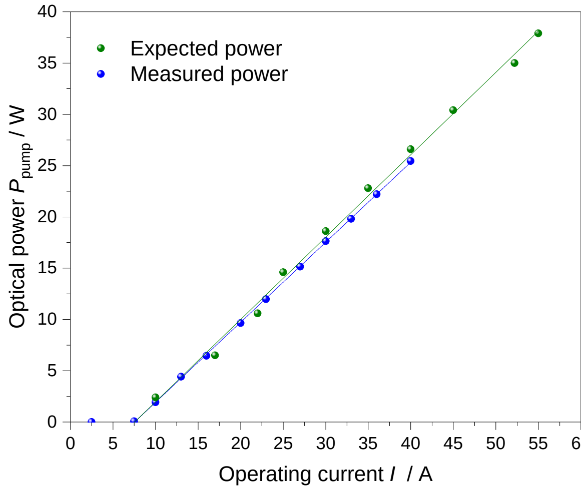

Figure 4.3.: Power measurement with a new fiber. The expected (blue) and the measured values (green) fit together.

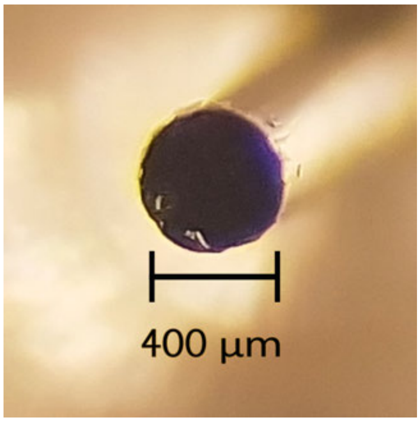

Figure 4.4.: A fiber end in good condition. It has a clear, round shape and no scratches on the surface.

The fit has the shape of a y-shifted line with the following values:

$$P_{\mathrm{pump}} = 0.780 \pm 0.004\, {}^{W}\!/\!{}_{A} \cdot I_{\mathrm{OP}} - 5.88 \pm 0.08\,\mathrm{W} \tag{4.1}$$

Due to the threshold the pump laser does not work below the current of $I_{\mathrm{TH}} = 7.54\,\mathrm{A}$.

4.2. Reflection of heatspreader and chip

A high energy density within the active region is necessary to achieve high output power and stable lasing. The incident beam gets reflected at each transition from one material to another. To obtain values about the reflection of the VECSEL chip and the heatspreader powermeter measurements were taken. The following results could be obtained by interpreting the slope of figure 4.5 as the ratio of reflectivity:

$$\mathrm{R_{SiC}} = 29.2\,\% \qquad \mathrm{R_{VECSEL}} = 22.8\,\% \qquad \mathrm{R_{Diamond+chip}} = 46.2\,\% \tag{4.2}$$

There are only two valid measurements for the VECSEL because it will be destroyed rapidly pumping without heatspreader. To make it possible to compare these values with the theory, the Fresnel equations (2.10) as well as Snell's law has been used to calculate the reflectivity from the refractive indexes.

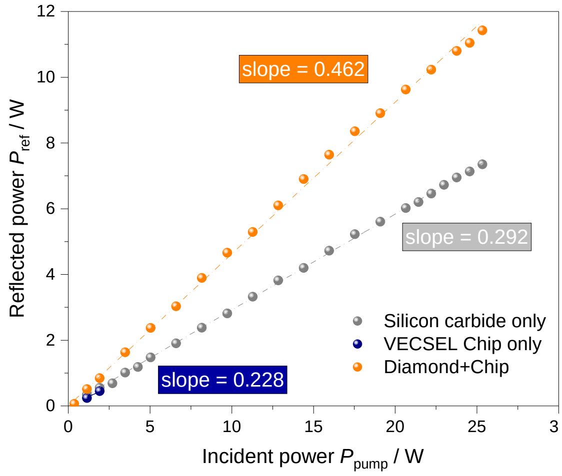

Figure 4.5.: Reflected power vs incident power for different materials. It is a strict linear behavior between the two variables. The slope is the ratio of reflected radiation to incident radiation.

The following refractive indexes are given at a wavelength of $\lambda = 888\,\text{nm}$ [18][19][20][21]:

$$n_{SiC} = 2.5953 \qquad n_{Diamond} = 2.3999 \qquad n_{GaAs} = 3.6040 + i \cdot 0.077749$$

The imaginary part of the reflectivity of GaAs is disregarded because it only affects a shift in frequency which does not influence the intensity of the reflection. SiC as well as diamond can be treated as dielectric and formula (2.11) is used to calculate the reflectivity. Since the pump laser light is non-polarized the arithmetic average of p- and s-polarized beam is taken. The refractive index of air is approximated with $n_{air} = 1$. The theoretical values for reflection are calculated for an incident angle of $\theta_i = 35^\circ$ except for the diamond/GaAs-transition where the emergence angle of diamond is used (calculated with Snell's Law) $\theta_{\text{i diamond}} = \theta_{\text{t GaAs}} = \arcsin\left({}^{n_{Air}}/_{n_{Diamond}} \sin(\theta i)\right) = 13.83^\circ$:

$$R_{SiC} = 0.199 \qquad R_{GaAs} = 0.320 \qquad R_{Diamond} = 0.173 \qquad R_{Diamond/GaAs} = 0.040$$

Obviously, the theoretical values do not fit to the experimental results because double- and multireflection is not considered right now. For multiple reflection between a layer structure of different materials the total reflectivity can be deduced to:

$$R_{\text{total}}(n) = \begin{cases} R_1 & ;\text{for } n = 1 \\ R_1 + (1 - R_1)^2 \sum\limits_{m=0} R_1^m R_2^{(m+1)} & ;\, m = n - 2;\ \text{for } n \geq 2 \end{cases} \tag{4.3}$$

Number of reflections	n	**Running index**	m
Reflection on layer one	R_1	**Reflection on layer two**	R_2

Applying the values on the formula, the total reflectivity does not change significant after three back reflections. A comparison between the measurements and this theoretical model does only make sense for SiC and the structure diamond/GaAs since there are no experimental measurements of one layer diamond or GaAs surrounded by air. For the named structures the reflection for multiple reflections is calculated using formula 4.3:

$$\mathrm{R}_{\text{SiC-Theo}} = 0.324 \qquad \mathrm{R}_{\text{Diamond/GaAs}} = 0.200$$

Comparing those results with the reflectivity of SiC (4.2) the approximation meets the experimental result. The diamond/GaAs structure differ by a factor of more than the double. This leads to the conclusion that the DBR of the VECSEL reflects a significant ratio of the incident radiation. A part of the transmitted light $T_{\text{Diamond/GaAs}} = 80\,\%$ which is not absorbed in the active region gets reflected at the DBR and in multiple reflections inside the chip structure. The rest can be assigned to the absorption inside the active region. Simulations suggest a transmittivity of less than $T \leq 2\,\%$. Therefore, this presumption is justified.

4.3. First alignment of the laser

To make sure that the mirror and the VECSEL are parallel to each other, a visible He-Ne low-power laser with $\lambda_{\text{Align}} = 632.8$ nm was used. The beam is guided along the axis between VECSEL and cavity mirror. When the cavity mirror is in the optical path, it creates a reflected dot that can be seen on the guiding mirror of the red alignment mirrors. By shifting position and angle of the cavity mirror, this dot can be moved. When the dot meets the point of the source, a interference pattern on the VECSEL chip is visible. This pattern is an indication for the correct alignment of the cavity.

4.3.1. Spontaneous emission

For the first PL measurements a green laser with the wavelength of $\lambda_{\text{Pump}} = 532\,\text{nm}$ and a power up to $P_{\text{pump}} = 6\,\text{W}$ was used. The visible light made the alignment easier and was sufficient for some first checks of the structure of our VECSEL-chip.

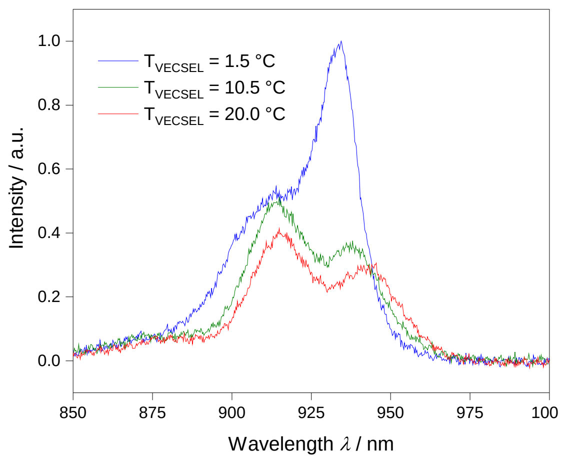

Figure 4.6.: PL measurements of spontaneous emission at different temperatures of the VECSEL. A pump laser with $P_{\text{pump}} = 80\,\text{mW}$ on a wavelength of $\lambda_{\text{pump}} = 532\,\text{nm}$ was used.

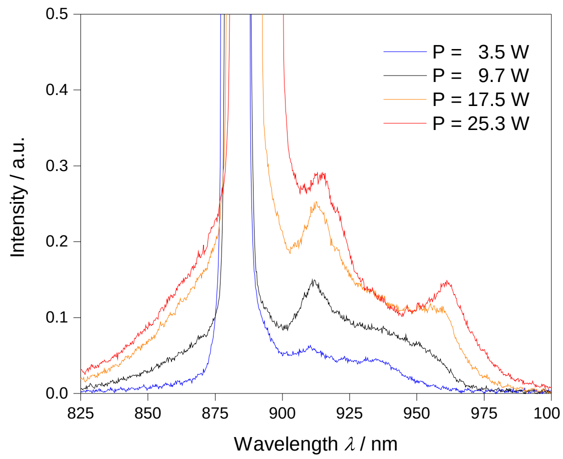

Figure 4.7.: PL measurements, pumping at a wavelength of $\lambda_{\text{Pump}} = 888\,\text{nm}$. Different pumping powers were used. The spectra are overlaid by the pump beam radiation. The chip temperature was $\theta_{\text{VECSEL}} = 10\,^\circ\text{C}$.

The green laser incidents at an angle of 30°. The chip temperature was varied from $T_{\text{chip}} = 1.5\,^\circ\text{C}$ to $T_{\text{Chip}} = 20\,^\circ\text{C}$. To obtain more light, a plano-convex lens was used to focus the emitted radiation into the spectrometer fiber. Figure 4.6 shows measurements that were made with a Thorlabs CCS200 spectrometer. It is determined by QW emission, DBR and subcavity resonances.

Figure 4.7 shows the measurements of spontaneous emission pumped with the diode laser intended for this setup. Four PL measurements were taken while increasing the current at the power supply. At this time, we had no edge filter to remove the pump beam radiation around $\lambda_{\text{Pump}} = 888\,\text{nm}$ from the measurement. Therefore, the spectra are overlaid by a peak at this wavelength. There is no visible redshift but obviously the emission increases with the pump power.

4.3.2. First stimulated emission

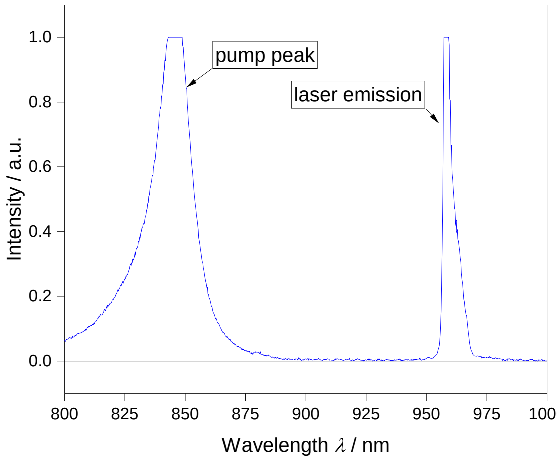

Figure 4.8.: PL measurements without any filters during first stimulated emission of the laser. Pumped at $\lambda_{\text{Pump}} = 888\,\text{nm}$ with a power of $P_{\text{Pump}} = 7.39\,\text{W}$. Clearly visible is the peak of the pump laser on the left.

After the pre-alignment of the infra-red diode laser some further shifts of the external mirror on different axes were made. Those attempts lead to the first stimulated emission of our VECSEL. Figure 4.8 shows the first PL measurements of stimulated emission in the setup that were made with the Thorlabs CCD200. The edge filter was demounted on this picture to show pump beam and stimulated emission together.

The temperature of the chip should be as low as possible but is limited by the dew point. If it drops below, there is the possibility of water condensation around the chip. This could influence the transmission behavior of the chip surface and may lead to oxidation of metallic parts of the construction. For a short measurement period it is problem but in continuous operation it would require a nitrogen ventilation. The inert gas with reduced humidity is forwarded to the chip and displaces the wet ambient air. However, this would step away from the plan of a simple setup. Measuring relative humidity and temperature, the dew point temperature in the laboratory could be approximated to $\theta_{\text{Dew}} = 6\,^{\circ}\text{C}$. Therefore, a temperature of $\theta_{\text{VECSEL}} = 10\,^{\circ}\text{C}$ is defined for continuous operation.

4.4. Laser characterization

4.4.1. Threshold power

The threshold power is an important characteristic of a laser because below this limit, stimulated emission is not given.

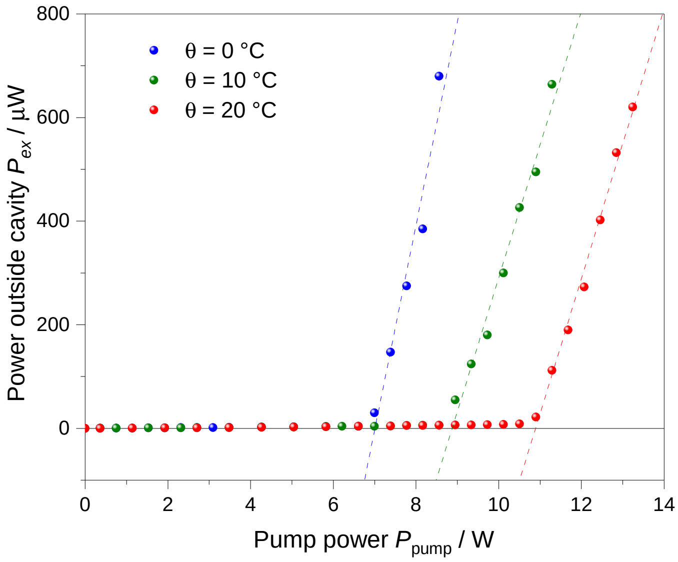

Figure 4.9.: Power of the extra cavity VECSEL output P_{ex} vs. the pump power P_{pump}. Below the threshold power which is determined by fitting with a linear function (dashed line) there is no stimulated emission.

Figure 4.9 displays the output power in the range where the laser is starting with stimulated emission. By using a linear fit, the threshold for the three temperatures could be determined to

$$P_{\mathrm{Thr;\,0^\circ C}} = 7.00\,\mathrm{W} \qquad P_{\mathrm{Thr;\,10^\circ C}} = 8.87\,\mathrm{W} \qquad P_{\mathrm{Thr;\,20^\circ C}} = 10.89\,\mathrm{W}$$

The threshold power drops at lower heatsink temperatures.

4.4.2. Output power

Figure 4.10 shows the output power of the VECSEL depending on the pump power. The output power was measured with a Thorlabs PM200. To avoid the influence of pump beam radiation, an edge filter was used.

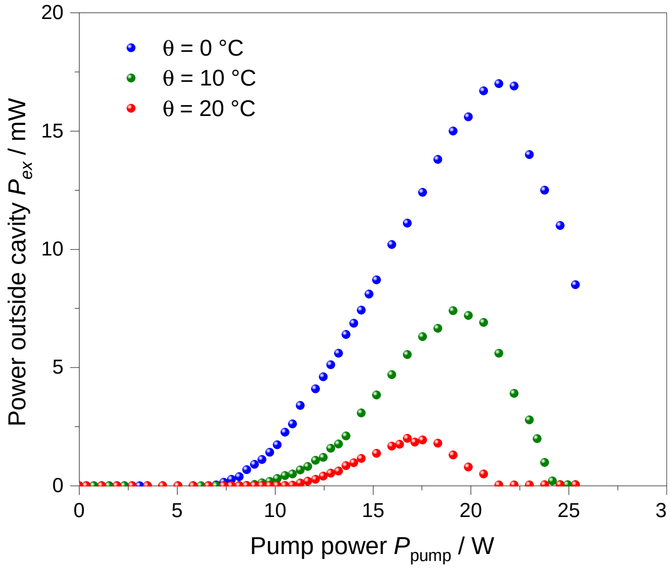

Figure 4.10.: Optical power of the VECSEL vs. pump power at three different temperatures. The HR-coated external cavity mirror leads to small external cavity powers. Due to a thermal rollover the maximum output power is not at the maximum of the pump power.

The temperature dependent maxima of the output power are:

$$P_{\text{Max; }0^\circ\text{C}} = 17.0\,\text{mW} \qquad P_{\text{Max; }10^\circ\text{C}} = 7.4\,\text{mW} \qquad P_{\text{Max; }20^\circ\text{C}} = 2.0\,\text{mW}$$

To achieve a high intra-cavity power for the SHG an extra cavity mirror with a reflective coating was used which is higher than usual. In the band of $\lambda_{\text{HR}} = 850\,\text{nm}$ to $1050\,\text{nm}$ 99.9 % of the incident radiation gets reflected. This means that the real inside-cavity power of our system is much higher. The fact that the maximum of the pump power does not coincide with the maximum of the outside power P_{ex} points on a phenomenon termed *thermal rollover*. The shape of the curve fits to the experiences other groups made with VECSEL lasers [22] [23] [7] (p. 272). In this state, the kinetic energy of the charge carriers inside the semiconductor is high enough to jump into the barriers where they recombine and the population inversion decreases. They are not available anymore for the stimulated emission. In addition, there is no photon that could have been emitted by this charge carrier and the feedback decreases. This vicious circle makes the laser collapse. The thermal rollover gets reached at lower pump powers as the temperature rises.

4.4.3. Temperature- and power-dependent frequency shift

An important parameter is the thermal shift which depends on the temperature. As the temperature increases, the charge carriers reach higher levels up to their kinetic energy. This causes a smaller energy gap between the bands and finally a longer wavelength. This phenomenon is also termed redshift. Figure 4.11 displays the shift which is caused by variation of the heat sink temperature. Additionally, the intensity decreases despite the same pump power level.

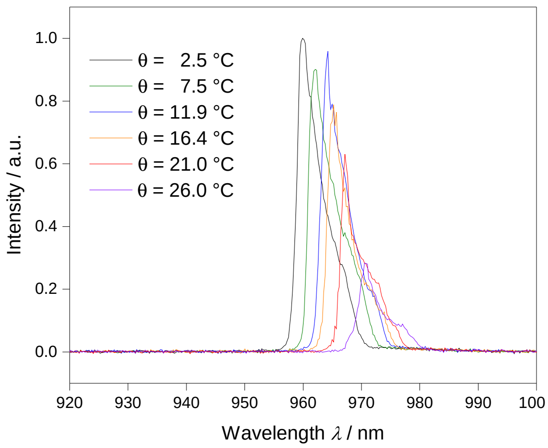

Figure 4.11.: PL measurements captured at a pumping power of P_{Pump} = 9.7 W at different VECSEL temperatures.

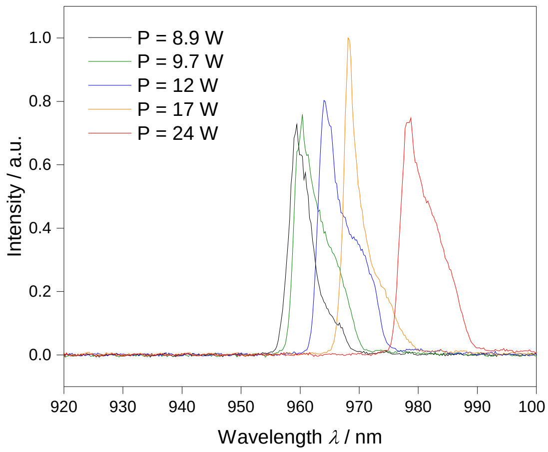

Figure 4.12.: PL measurements at different pumping currents at the same temperature θ = 10 °C. A steady shift which goes with the pump power is visible.

The power dependent frequency shift (figure 4.12) gives information about the heat dissipation in the system. The shift depends on the temperature of the active region. If the heat which is produced by the incident pump beam is not dissipated, the active region warms up. This causes a smaller bandgap and finally the wavelength increases.

4.4.4. Thermal resistance

To get some further information about the thermal behavior in our system, the thermal resistance is calculated as a comparable scale for the thermal dissipation. Therefore, we determine and plot the peak positions for the different pump powers and temperatures (figure 4.13). We assume a linear behavior for the frequency shift by fitting the peak position with a linear function. Now we have the thermal- respectively power-dependent alteration rate which goes into the formula of the thermal resistance.

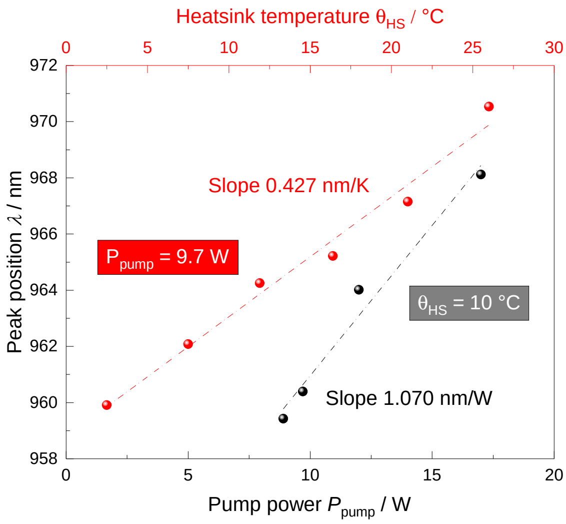

Figure 4.13.: Wavelength position dependent on the pump power respective heatsink temperature. The dashed line is the linear fit which gives the slope of the measurement.

The equation for the thermal resistance is given by [24]:

$$R_{\mathrm{th}} = \frac{\partial\lambda}{\partial P_{\mathrm{pump}}} \Big/ \frac{\partial\lambda}{\partial T} \Big|_{P_{\mathrm{pump}} = \mathrm{const.}} \tag{4.4}$$

We insert the slope of the linear fits in figure 4.13:

$$R_{\mathrm{th}}(T_{\mathrm{hs}} = 10\,^{\circ}\mathrm{C}) = \frac{1.070\,\mathrm{nm/W}}{0.427\,\mathrm{nm/K}} = 2.5\,\mathrm{K/W} \tag{4.5}$$

This is already a pretty good value compared to the simulations and measurements made with a barrier pumped 660 nm-VECSEL and diamond heatspreader, using a precursor of our heatsink [25]. The thermal resistance could be investigated to $R_{\mathrm{th}}(T_{\mathrm{hs}} = -28\,^{\circ}\mathrm{C}) \approx 4.8\,\mathrm{K/W}$ and $R_{\mathrm{th}}(T_{\mathrm{hs}} = 16\,^{\circ}\mathrm{C}) \approx 7.2\,\mathrm{K/W}$. The lower this value is, the more heat gets dissipated. The thermal resistance is expected to be considerably improved with the diamond heatspreader and the new heatsink (see section 6.1 and 6.2).

4.4.5. Heat output

The heat output that must be dissipated by the heatspreader depends on the reflection of the incident pump beam and the quantum defect. The latter is a scale for the part of absorbed energy which transits into heat.

$$q = \frac{E_{\text{pump}} - E_{\text{laser}}}{E_{\text{pump}}} = 1 - \frac{\lambda_{\text{pump}}}{\lambda_{\text{laser}}} \tag{4.6}$$

Energy of the pump wavelength	E_{pump}	**Energy of the laser wavelength**	E_{laser}
Conversion coefficient	Γ	**Wavelength of pump/laser**	$\lambda_{\text{pump/laser}}$

The quantum defect is calculated by the pump wavelength and the emitted laser wavelength at full pump power (see chapter 4.4.3).

$$q = 1 - \frac{888\,\text{nm}}{979\,\text{nm}} = 9.3\,\% \tag{4.7}$$

The reflectivity of VECSEL and heat spreader is determined in section 4.2 to $R_{\text{Diamond+chip}} = 46.2\,\%$. The heat output is the part of the beam which is not reflected by the chip, multiplied with the ratio of quantum defect. With a maximum pump power $P_{\text{pump}} = 25\,\text{W}$ the heat output is calculated to $P_{\text{heat}} = 1.25\,\text{W}$.

In practice this value is slightly higher due to radiation-free recombination inside the VECSEL which is not considered in this calculation.

5. Summary

In the frame of this thesis it was possible to get the VECSEL chip to a stable lasing. A series of pioneering measurements could be carried out on the system.
The extra cavity power at the corresponding temperature dependent wavelength in the infra-red could be assumed to a maximum of $P_{Max;\,0^{\circ}C} = 17.0\,mW$. Due to a reflectivity of the external cavity mirror of $R_{M\,Ext} \leq 99.9\,\%$ it can be predicted that the intracavity power is quite higher. The maximum power is limited by the thermal rollover, a state in which the thermal energy is sufficient to lift the charge carriers into barriers where they are not available to supply the stimulated emission anymore. At various points, solutions for raising this limit have been found and initiated. The thermal dependent frequency shift as well as the pump power dependent frequency shift of the system were investigated. Furthermore, the results were used in the calculation of the Lyot filter and the design of an optimized chip structure. In addition, as a guideline for later measurements, the thermal resistance of the system was calculated.

6. Outlook

After we succeeded in setting up a linear cavity, the next step is to setup a V-shaped cavity. This provides the option to insert a BBO crystal and get a frequency doubling which was not possible in the linear cavity due to the absorption of the SHG in the VECSEL chip material. Furthermore, some extensive improvements were initiated. This includes a new chip design, the design of a mount for a rotatable birefringent filter and some pending measurements with a diamond heat spreader which are already prepared but could not be conducted in the frame of this thesis.

6.1. Diamond heatspreader

Both the thermal rollover described in section 4.4.2 and the excessive power-dependent frequency shift (figure 4.12) indicate that there are problems with the dissipation of resulting heat. The pump beam incidents from the top. That is why most of the heat is created there and improvements promise the most benefit. Figure 6.1 shows the results of measurements made with a 920 nm-VECSEL-system, QW-pumped with $P_{\text{pump}} = 24\,\text{W}$ at $\lambda_{\text{pump}} = 808\,\text{nm}$ [26]. The group around Ki-Sung Kim achieved an output power of $P_{\text{output}} = 12\,\text{W}$ with a slope efficiency as high as 58 % by optimization of the gain structure and the use of diamond heatspreader. The power limits they had with SiC heatspreader which look very similar to our output-power behavior (figure 4.10) disappeared as they switched to diamond [26]. Therefore, it is expected to improve the thermal dissipation in our setup significantly if a diamond heatspreader is used instead of SiC.
It is important that the diamond is monocrystalline to not influence the polarization of the transmitting radiation. Such diamonds are extremely difficult to obtain because they need a sophisticated manufacturing due to their extraordinary purity. Thanks to kind support by the IHFG, especially Roman Bek, we are lucky to have such a diamond heatspreader which is already built in and ready for measurements that are still pending.

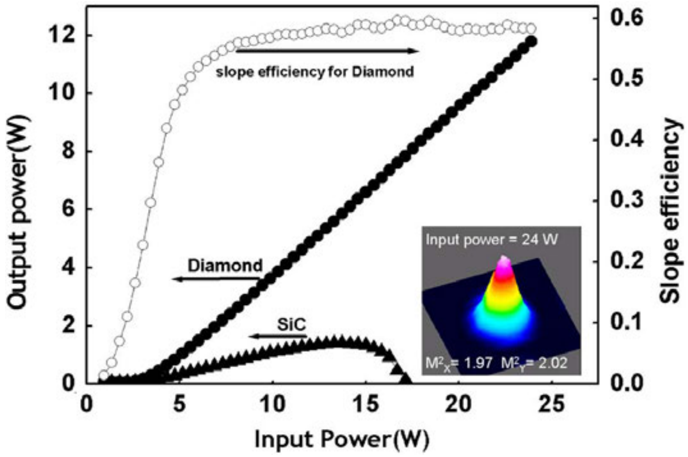

Figure 6.1.: Output power of a $\lambda_{\text{pump}} = 808\,\text{nm}$-pumped VECSEL, emitting at $\lambda_{\text{output}} = 920\,\text{nm}$. Two heat spreader materials, SiC and diamond are compared concerning their thermal dissipation. Taken from [26].,

6.2. Design of the heatsink

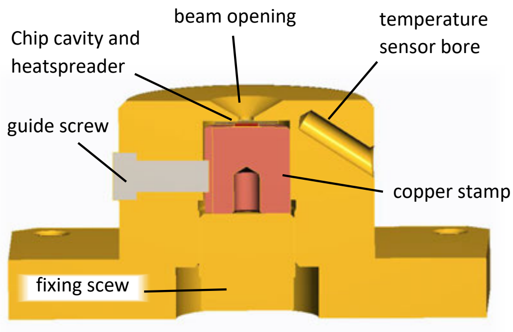

Figure 6.2.: Rendered picture of the new version of the heatsink. The Top part consists of one solid piece. This leads to a better thermal conductivity. Heatspreader and VECSEL are fixed from the bottom with a copper stamp.

As part of the experiments which are running at the IFHG, an existing design of a heatsink could be used for our experiments. During the period of measuring the need for an optimized design has increased. Some problems which expected to be solved with the new design are described below.
The VECSEL chip had to be replaced more than three times during the practical time of this bachelor thesis. Despite all parts were handled with care, the unique SiC heatspreader crushed during a bonding process. There were no spare parts available with the right size $\varnothing_{\text{SiC}} = 4\,\text{mm}$. The on-stock SiC-plates at the IFHG have a diameter of $\varnothing_{\text{SiC}} = 8\,\text{mm}$. This size is not suitable with the design of the actual heatspreader because of the two arrestor pins which keep the pressure disk in place (see figure 6.2). Cutting out SiC parts to make them fit is only possible with high-power laser cutters like those, that are used at the IFSW[1] at the University of Stuttgart. Anyway, cutting an existing $\varnothing_{\text{SiC}} = 8\,\text{mm}$ wafer is not economic. The new design

[1] **I**nstitut **f**ür **S**trahl**w**erkzeuge

makes is possible to supply heatspreaders in a wide range from $\varnothing_{\mathrm{SiC}} = 3\,\mathrm{mm}$ up to $\varnothing_{\mathrm{SiC}} = 10\,\mathrm{mm}$. Furthermore, the thermal contact of the existing heatspreader with the screw nut on the topside of the chip has some disadvantages in thermal conduction. The higher ratio of the thermal energy is created on the top of the chip where the screw nut is located. The screw nut made of brass has worse contact to the heat sink due to the thread between the two parts. A design of the heatsink which conducts the heat as one complete part to delay thermal rollover (see chapter 4.4.2) is preferable. In addition, the Pt100 thermoelement is placed inside the copper heat pipe, far behind the chip. An adequate and time actual result in the measurement of temperature is not given. The new design which was invented in cooperation with Alexander Peschken from the IFHG promises improvement for all the mentioned problems. The new components are already in production but not finished at this time.

6.3. Birefringent filter

As the functional principle describes in chapter 2.3, the birefringent filter allows to tune the transmitting wavelength in a certain range. Due to the results obtained in this bachelor thesis it is possible to approximate the shift, that is necessary to compensate the redshift caused by the heat to $\lambda_{\mathrm{Shift}} \approx 10\,\mathrm{nm}$. Having those values, the thicknesses of the plates which are relevant for the tuning range can be calculated. Finally, it is possible to design the holder that has to support the corresponding plates and the ability to rotate them in a defined angle. The Design for the birefringent filter holder is initiated but still pending.

Appendix

A. Epitaxy structure

Layer sequence of the VECSEL-Chip used in this thesis (Sample no. W00735) [4]

Material	Thickness	Comment	
GaAs	58.3 nm	Capping layer	
$Al_{30\%}GaAs$	17 nm	Spacer	
$Ga_{6\%}AsP$	18 nm	Barrier	5x
$In_{13\%}GaAs$	8 nm	QW	
$Ga_{6\%}AsP$	16 nm	Barrier	
$In_{13\%}GaAs$	8 nm	QW	
$Ga_{6\%}AsP$	16 nm	Barrier	
$In_{13\%}GaAs$	8 nm	QW	
$Ga_{6\%}AsP$	16 nm	Barrier	
$In_{13\%}GaAs$	8 nm	QW	
$Ga_{6\%}AsP$	18 nm	Barrier	
$Al_{30\%}GaAs$	17 nm	Spacer	
GaAs	936 nm	Barrier	
GaAs	65.3 nm	DBR	30x
AlAs	78.6 nm	DBR	
GaAs	100 nm	Buffer	
GaAs	350 μm	Substrate (110) 6° $\longrightarrow$ [111]	

B. Technical drawing of the heatsink

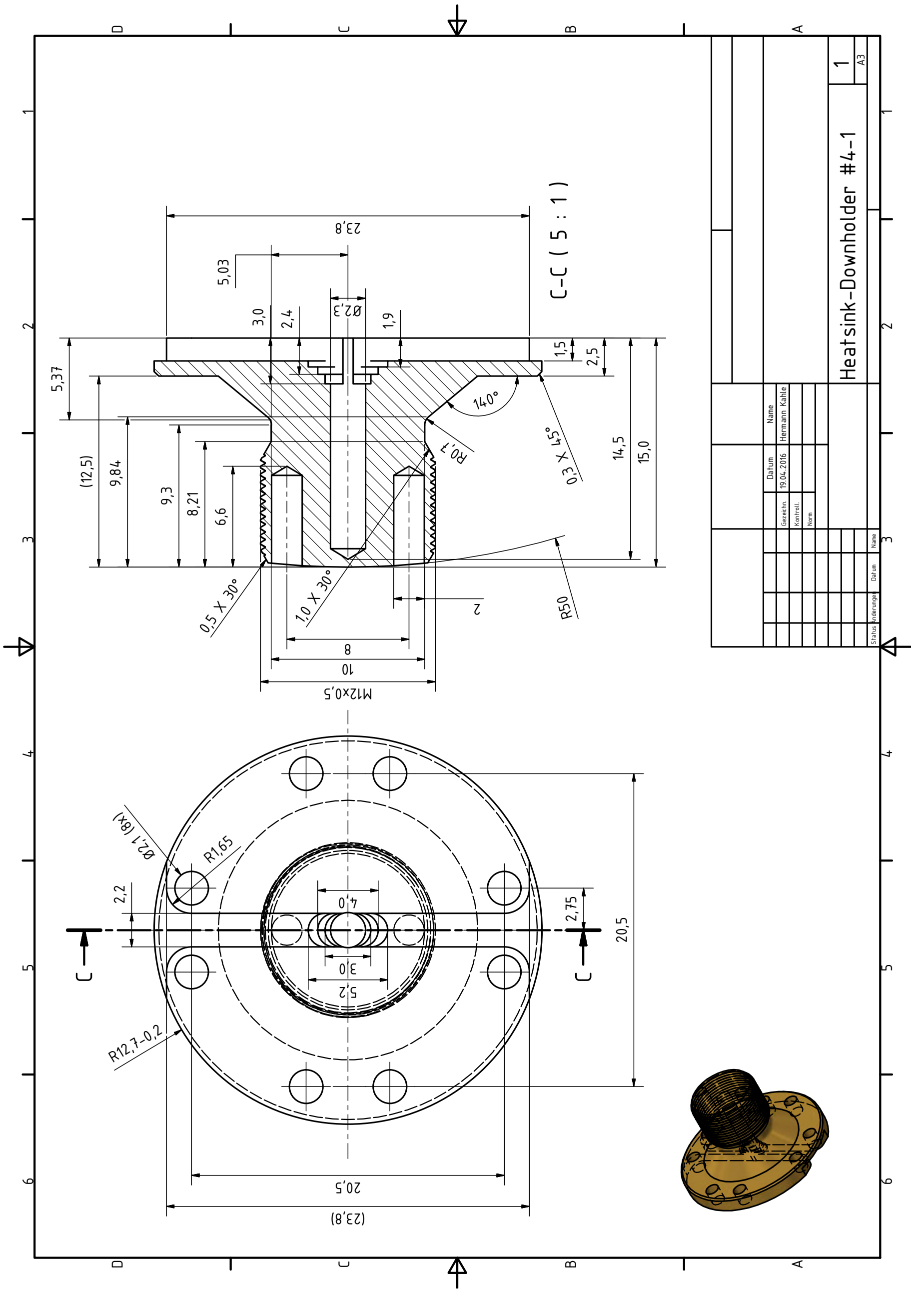

Figure B.1.: Technical drawing of the heatsink-downholder used in our setup. Kindly provided by Roman Bek from the IHFG.

C. Revised version of the heatsink

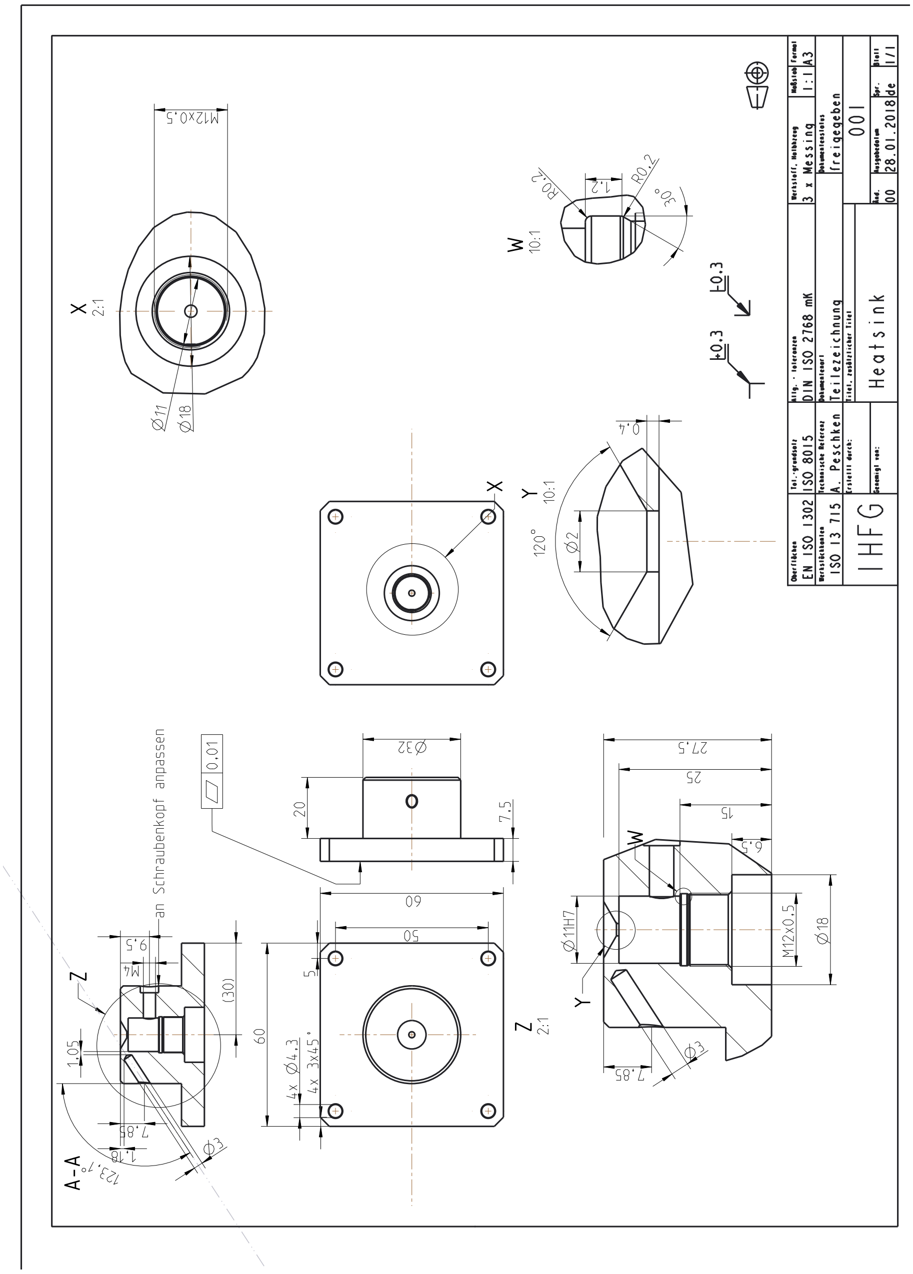

Figure C.2.: Technical drawing of the heatsink-downholder used in our setup. Kindly provided by Alexander Peschken from the IHFG.

List of Figures

Bibliography

[1] S. Nakamura, S. J. Pearton, and G. Fasol, *The blue laser diode: the complete story.* Physics and astronomy online library, Berlin: Springer, 2., updated and extended ed. ed., 2000. UB Vaihingen.

[2] C. Czeranowsky, E. Heumann, and G. Huber, "All-solid-state continuous-wave frequency-doubled nd:yag–bibo laser with 2.8-w output power at 473 nm," *Opt. Lett.*, vol. 28, pp. 432–434, Mar 2003.

[3] A. Hein *et al.*, "Efficient 460-nm second-harmonic generation with optically pumped semiconductor disk lasers," *IEEE Photonics Technology Letters*, vol. 23, pp. 179–181, Feb 2011.

[4] R. L. Hermann, "Entwicklung eines Halbleiter-Lasers für die Atomspektroskopie," 2017.

[5] A. L. Schawlow and C. H. Townes, "Infrared and optical masers," *Phys. Rev.*, vol. 112, pp. 1940–1949, Dec 1958.

[6] H. Haken and H. C. Wolf, *Atom- und Quantenphysik: Einführung in die experimentellen und theoretischen Grundlagen.* Springer-Lehrbuch, Berlin ; Heidelberg: Springer, achte, aktualisierte und erweiterte auflage ed., 2004. UB Stadtmitte.

[7] D. Meschede, *Optics, Light and Lasers: the practical approach to modern aspects of photonics and laser physics.* Weinheim: Wiley-VCH Verlag GmbH & Co. KGaA, 2004. UB Vaihingen.

[8] Laser Quantum Ltd, "Model Finesse 5 W." "`laserquantum.com/products/detail.cfm?id=33`".

[9] D. Eimerl *et al.*, "Optical, mechanical, and thermal properties of barium borate," *Journal of Applied Physics*, vol. 62, no. 5, pp. 1968–1983, 1987.

[10] J. A. Sedlacek, A. Schwettmann, H. Kübler, R. Löw, T. Pfau, and J. P. Shaffer, "Microwave electrometry with rydberg atoms in a vapour cell using bright atomic resonances," *Nature Physics*, vol. 8, no. 11, p. 819, 2012.

[11] E. Hecht, *Optik.* Studium, München: De Gruyter, 6., verb. aufl. ed., 2014. UB Vaihingen.

[12] Thorlabs, "DCC1545M USB CMOS Camera, Monochrome." "`Thorlabs.com/thorProduct.cfm?partNumber=DCC1545M`". Sensor specifications in the manual (page 445).

[13] H. P. Kahle, *AlGaInP-based high-performance semiconductor disc lasers for the red spectral range.* PhD thesis, IHFG - University of Stuttgart, 2016.

[14] Deutsches Kupferinstitut, “Kupfer-Zink-Legierungen, Informationsdruck i.5, Auflage 03/2007.” "www.kupferinstitut.de".

[15] H. H. Binder, *Lexikon der chemischen Elemente: das Periodensystem in Fakten, Zahlen und Daten; mit 96 Abbildungen und vielen tabellarischen Zusammenstellungen.* Stuttgart; Leipzig: Hirzel, 1999. UB Vaihingen.

[16] K. Takahashi, A. Yoshikawa, and A. Sandhu, eds., *Wide Bandgap Semiconductors: Fundamental Properties and Modern Photonic and Electronic Devices.* SpringerLink : Bücher, Berlin, Heidelberg: Springer Berlin Heidelberg, 2007.

[17] Z. L. Liau, “Semiconductor wafer bonding via liquid capillarity,” *Applied Physics Letters*, vol. 77, no. 5, pp. 651–653, 2000.

[18] S. Singh, J. R. Potopowicz, L. G. V. Uitert, and S. H. Wemple, “Nonlinear optical properties of hexagonal silicon carbide,” *Applied Physics Letters*, vol. 19, no. 3, pp. 53–56, 1971.

[19] H. R. Phillip and E. A. Taft, “Kramers-kronig analysis of reflectance data for diamond,” *Phys. Rev.*, vol. 136, pp. A1445–A1448, Nov 1964.

[20] S. Ozaki and S. Adachi, “Spectroscopic ellipsometry and thermoreflectance of gaas,” *Journal of Applied Physics*, vol. 78, no. 5, pp. 3380–3386, 1995.

[21] M. N. Polyanskiy, “Refractive index database.” https://refractiveindex.info. Accessed on 2018-02-15.

[22] B. Heinen *et al.*, “106 w continuous-wave output power from vertical-external-cavity surface-emitting laser,” *Electronics Letters*, vol. 48, pp. 516–517, April 2012.

[23] A. Kemp *et al.*, “Thermal lensing, thermal management and transverse mode control in microchip vecsels,” *Applied Physics B*, vol. 83, p. 189, Mar 2006.

[24] B. Heinen *et al.*, “On the measurement of the thermal resistance of vertical-external-cavity surface-emitting lasers (vecsels),” *IEEE Journal of Quantum Electronics*, vol. 48, pp. 934–940, July 2012.

[25] T. Schwarzbäck, *Epitaxie AlGaInP-basierter Halbleiterscheibenlaser: Dauerstrichbetrieb, Freuqenzverdopplung und Modenkopplung.* PhD thesis, IHFG - Uni Stuttgart, 2013.

[26] K.-S. Kim *et al.*, “920-nm vertical-external-cavity surface-emitting lasers with a slope efficiency of 58% at room temperature,” *IEEE Photonics Technology Letters*, vol. 19, no. 20, pp. 1655–1657, 2007.